ADVANCED MATERIALS INTERFACES

www.advmatinterfaces.de

Effect of Perforation on the Thermal and Electrical Breakdown of Self-Rolled-Up Nanomembrane Structures

*Julian A. Michaels, Derek R. Wood, Paul J. Froeter, Wen Huang, Dane J. Sievers, and Xiuling Li**

Strain-induced self-rolled-up membranes (S-RuM) are structures formed spontaneously by releasing a strained layer or layer stacks from its mechanical support, with unique applications in passive photonics, electronics, and bioengineering. Depending on the thermal properties of the strained layers, these structures can experience various thermally induced deformations. These deformations can be avoided and augmented with the addition of strategically placed perforations in the membrane. This study reports on the use of perforations to modify the thermal effects on strained silicon nitride S-RuM structures. A programmable fuse with well-defined thermal threshold, ultrasmall footprint, and 2–3 V voltage rating is demonstrated, which can potentially serve as an on-chip sensing device for power electronic circuits.

In recent years the prevalence of microtubes in research has grown tremendously because of their wide range of applications.[1–11] Strain-induced Self-Rolled-up Membranes (S-RuM) are of great interest due to their CMOS-compatible planar fabrication process and versatile 3D architectures produced by self-assembly. S-RuM tubular structures have been used to fabricate miniaturized passive electronic and photonic components, such as inductors,[6,11,12] capacitors,[7] transformers,[12,13] and waveguides.[14–17] S-RuM structures are formed by releasing a strained bilayer from a sacrificial layer, resulting in a tubular structure comprised exclusively of the bilayer material. One of the primary advantages of fabricating these passive electronics on the S-RuM platform is the ability to engineer the membrane structure on which they are constructed in 2D before rolling-up into a 3D architecture with versatile classes of materials. Some common choices of the dielectric bilayer include SiN_x,[13,18] SiO_x,[3,4] Al_2O_3,[19] ZnO,[3] and TiO_2.[20,21]

The performance of these electrical devices is ultimately limited by the layer's thermal handling capability because they tend to deform and collapse under thermal stress.[2] It has been shown that the addition of controlled perforations on S-RuM structures allows manipulation of shapes;[2] however, this effect is not sufficiently understood to incorporate perforations in device structures. This article examines these physical effects in a strained SiN_x bilayer as a function of temperature. Various structures with different perforation patterns and lengths are presented with the goal of formulating strategic inclusion of pores in strained bilayer structural design.

Four types of SiN_x membrane structures consisting of partially and fully perforated patterns have been explored. **Figure 1**a–d shows the rolled-up microtubes with their corresponding planar perforation patterns illustrated in Figure 1a′–d′ and the rolling direction labeled. All the perforated structures have the same 2D dimensions, 61 μm wide and 17 μm long rectangular strips. Figure 1a–c shows structures with 2 μm diameter pores spaced by 2 μm square lattice distributed evenly, gradually, and abruptly across the membrane for a total of 16.2%, 10.8%, and 5.4% area porosity, respectively. The structure in Figure 1d has arrays of 12 μm × 2 μm rectangular slits with the longer side oriented along the circumference of the tube. All of these perforation patterns did not change the rolling behavior compared to the solid membrane with no pores. The resulting tubes are all single turn with a diameter of ≈5 μm within experimental error. Tubes with multiple turns were studied, though their reduction characteristics varied greatly depending on the number of their turns. Perforations were chosen to be 2 μm as that is the lower limit of the available lithography equipment and would allow for more precise control of perforation density. Larger perforations would not roll straight consistently due to the etching characteristics of the sacrificial layer. Given the length of the tubes, spacing could not be varied significantly and longer perforations (with width of 2 μm) could not be fit on the tube symmetrically, without catastrophically impacting rolling.

When subjected to rapid thermal annealing (RTA), the tube showed little or no signs of change in shape or diameter initially. As the annealing temperature increases, the tube geometry starts to change in the form of diameter reduction. **Figure 2**a plots the inner diameter reduction (left axis) and actual diameter value (right axis) of the annealed tubes as a function of annealing temperature, in the range of 300–650 °C, for both the unperforated solid (black trace) and the uniformly perforated tubes (red trace). The temperature dependence of the diameter reduction experiences a threshold-like behavior where a sudden dramatic change takes place before transitioning into gradual

J. A. Michaels, D. R. Wood, P. J. Froeter, W. Huang, D. J. Sievers, X. Li
Department of Electrical and Computer Engineering
Micro and Nanotechnology Laboratory
Materials Research Laboratory
University of Illinois at Urbana-Champaign
Urbana, IL 61801, USA
E-mail: xiuling@illinois.edu

The ORCID identification number(s) for the author(s) of this article can be found under https://doi.org/10.1002/admi.201901022.

DOI: 10.1002/admi.201901022

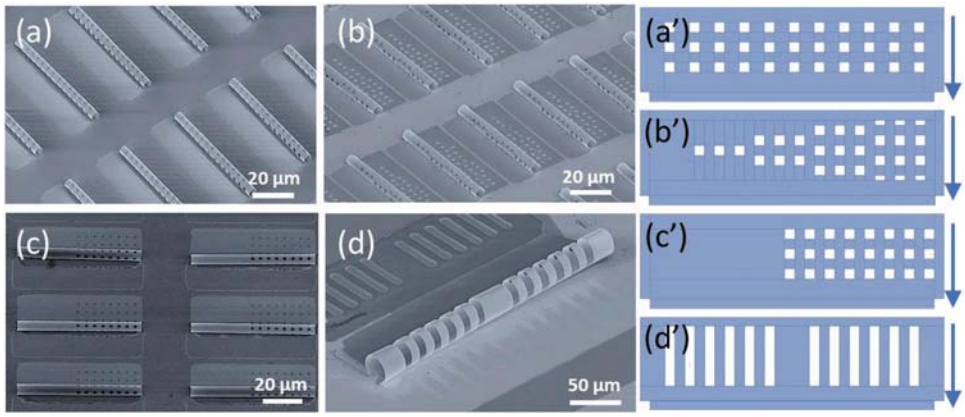

Figure 1. Arrays of SiN_x microtubes self-rolled up from 2D sheets with different perforation patterns. a) uniform square lattice perforations; b) gradient perforations; c) abrupt one-sided perforations; d) rectangular perforations; The corresponding 2D patterns are shown on the right as (a′), (b′), (c′), and (d′), respectively, with the arrow indicating rolling direction.

reduction with continued rise in temperature. The threshold temperature is 460 and 580 °C for the solid and perforated tubes, respectively. The corresponding tube geometries before and after annealing at their respective threshold temperatures are shown in Figure 2b–e, as indicated. The diameter shrinking of the originally single-turn tube leaves the inner edge of the membrane free room to wrap further into a multiturn tube. Each turn has uniform diameter across the length of the tube. The solid tube now rolled-up into ≈1.5 turns (Figure 2c), with the inner diameter reduced to 2.5 from 5 μm (ΔD = 50 ± 4.51%); while the inner diameter of the perforated one reduced even more dramatically to 1.7 μm (ΔD = 66 ± 4.17%) at its corresponding threshold temperature (Figure 2e), resulting in more than two turns, although there are noticeable gaps in between turns. These gaps were generated because the base of the tube more efficiently dissipates heat than the top does (furthest along the tube), meaning that the top experiences more thermal exposure and therefore more diameter reduction than the base. Beyond the threshold temperature, the reduction of diameter gradually increased and leveled off at approximately 85% and 75% total reduction for the solid and the perforated tubes, respectively. Clearly, the perforated tubes possess higher thermal stability than the solid tubes, as shown in the much higher threshold temperature for physical deformation and larger amount of total change in diameter.

As expected, the tube with the gradually perforated geometry with the perforations distributed along the tube length (Figure 1b), exposed to T_a = 580 °C annealing, turned into a cone shape with more reduction in diameter on the more solid side and tapered to less reduction on the more perforated side. Detailed characterization of the diameter reduction measured along the tube segmented in five sections are plotted in Figure S1 in the Supporting Information. Similarly, for the tube geometry with half solid and half perforated area (Figure 1c), there was the predictable trend of higher thermal stability in perforated sections than the more solid sections; however, the exact

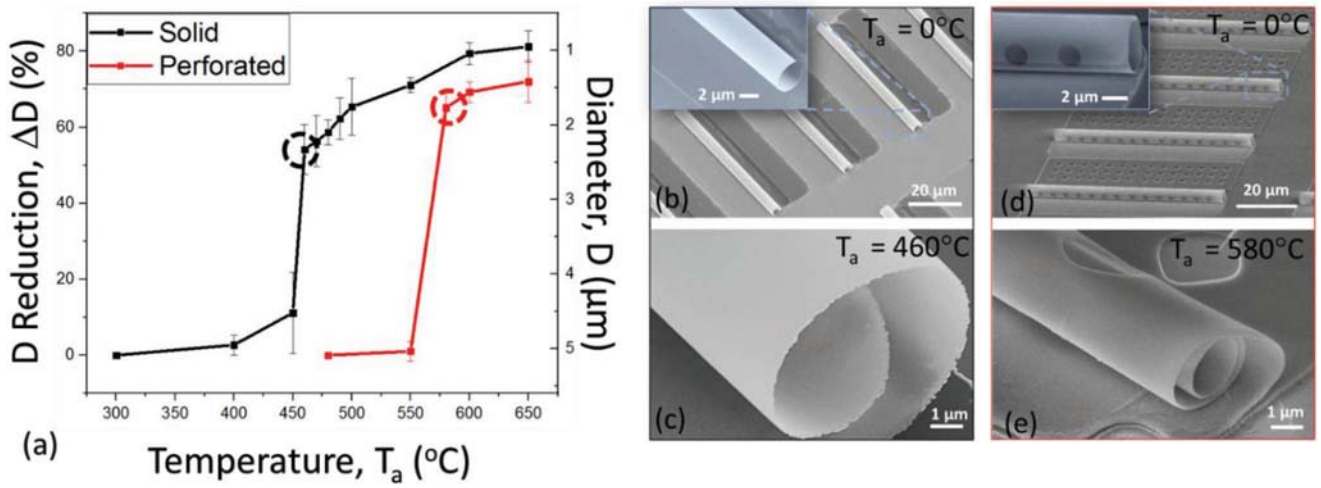

Figure 2. a) Plot of the percentage of inner diameter reduction of SiN_x S-RuM microtubes as a function of annealing temperature for the solid (black) and fully perforated (red) microtubes. The circled points represent the threshold of diameter reduction. SEM images of b,c) solid microtubes (b) before (no T_a) and (c) after annealing at 460 °C, respectively; d,e) fully perforated microtubes (d) before and (e) after annealing at 580 °C. Insets in b,d) show zoomed-in images of the end of a rolled tube to compare with the after annealing image in c,e), respectively.

values of diameter are not exactly matching those in their perforated S-RuM and solid S-RuM cases. Overall, the reduction values are more averaged, that is, in Section 1 reduction was 46.0% (Figure S1, Supporting Information), while the perforated S-RuM reduction was 38.0% (Figure 2e), and in Section 2 reduction was 73.3% (the inner roll), while the solid S-RuM reduction was approximately 76.1%. Data for these structures can be found in the Supporting Information (Pages 2–3).

The thermal effect of these nonuniformly perforated structures further confirms the thermal resistance correlation with perforation on the rolled nanomembrane microtube walls. With more perforations, either locally or globally, S-RuM tubular structures can withstand higher temperatures and experience a smaller reduction in diameter. As shown in Figure S2 in the Supporting Information, microtubes with large, vertically oriented rectangular perforations, corresponding to those in Figure 1d collapsed after thermal treatment at 580 °C. The hypothesis would suggest that more or larger perforations would correspond to a higher thermal threshold, but after treatment at 580 °C, the tubes collapsed, demonstrating a boundary to this theory. Such catastrophic shape deformation is likely the result of mechanical breakdown during thermal deformation transient for such a hollow structure. In short, without sufficient material in the tube the correlation between increasing perforation density and thermal threshold no longer holds.

Similar to the single turn tubes, those with multiturns also showed diameter reduction in general upon thermal annealing, however the trend of reduction is not well defined, probably due to the geometrical restriction to physical deformation and the thermal mass difference. Nonetheless, perforation also increases the thermal stability of tubes with multiple turns.

As previously reported,[22,23] although the SiN_x deposited using a $NH_3/SiH_4/N_2$ PECVD process contains an amine-rich hydrogenated amorphous film with nonstoichiometric composition, upon exposure to sufficiently high temperature, it partially reduces to Si_3N_4, as illustrated in the chemical reaction Equations (1) and (2) shown below. Compressive stress is generated by a denser film formed with ion bombardment taking place during low-frequency (LF) deposition.[2,22,24,25] Tensile strain is generated primarily from [Si—N] bonds interaction, which occurs more during high-frequency (HF) deposition condition; these bonds' dominance is caused by the smaller mean free path of the radicals generated by the plasma.[26] Therefore, the tensile strain in the SiN_x layer is correlated to the average molecular distance in the layer.[22,27,28] When the annealing temperature is sufficiently higher than the film deposition temperature, the hydrogen and ammonia byproducts diffuse out and leave more [Si—N] bonds causing a decrease in compressive stress and an increase in tensile strain, respectively, in both of the layers.[22,26,28] This increase in tensile strain is most prevalent in the HF SiN_x layer and the overall differential of stress between the two layers therefore increases significantly. An increase in net stress leads to a change in geometry and, in the case of these SiN_x S-RuM tubes, diameter reduction.[2,24] Not all the SiN_x reduces to Si_3N_4 all at once as described in Equations (1) and (2); the process is a function of thermal exposure. In the limit of pure Si_3N_4, with stress dominated by [Si—N] bonds, the layer's tensile stress is maximized,[29] leading to total collapse in the tubes presented here due to the lack in strain difference between the bilayers

Table 1. Film stress measured before and after RTA, with percent change in film stress and standard deviations indicated.

Film	Film stress pre-anneal [MPa]	Film stress post-anneal [MPa]	Percent change [%]
20 nm LF SiN_x	−1195 ± 44.7	−1109 ± 33.3	7.2%
20 nm HF SiN_x	415 ± 29.2	873 ± 29.4	110%

$$SiH_4(g) + 4NH_3(g) \xrightarrow{\text{Plasma}} Si(NH_2)_4(s) + 4H_2(g) \quad (1)$$

$$3Si(NH_2)_4(s) \xrightarrow{T_a > 300\,^\circ C} Si_3N_4(s) + 8NH_3(g) \quad (2)$$

Shown in **Table 1** is the film stress measured before and after annealing from the control experiments using single layer planar SiN_x films. It can be seen that while the annealing only reduced the compressive stress LF layer by 7.2%, the tensile stress dramatically increased by 110% in the HF layer. We note that compared to the rolled-up structures, the annealing effect on these control samples that are planar film supported by a substrate will likely behave differently in terms of the order of magnitude. Nonetheless, the trend of increase in tensile strain prevalent in the HF SiN_x layer, hence overall increase of differential stress, is consistent with the reduction of diameter in the rolled-up structures.

Our results show that thermal stability of perforated S-RuMs is higher than that of their nonperforated counterparts. Presumably, this characteristic is related to the thermal resistivity of the structure, which can be modelled as a hollow tube, and the thermal resistivity of which can be described with Equation (3)[30]

$$R_{\text{thermal}} = \left(\frac{1}{k}\right)\frac{\ln\left(\frac{r_1}{r_0}\right)}{2\pi L_{\text{tube}}} \quad (3)$$

where R_{thermal} denotes the thermal resistance of the tube, k, a physical constant corresponding to the material thermal conductivity, 1.18 W m^{-1} K^{-1} as previously reported,[31] r_0 and r_1, the inner and outer radii, respectively, and L_{tube}, the tube length. The thermal resistance is inversely proportional to the surface area and has a weak dependence on the tube thickness.

We can infer, by accounting for the loss of surface area in the form of perforation, that the thermal resistance of a uniformly perforated tube can be represented by Equation (4)

$$R_{\text{thermal}} = \left(\frac{1}{k}\right)\frac{\ln\left(r_1/r_0\right)r_{\text{tube}}}{2\pi r_{\text{tube}}L_{\text{tube}} - N_{\text{p}}A_{\text{p}}} \quad (4)$$

where r_{tube} represents the average radius of the tube, A_{p} the area of each perforation, and N_{p} the number of holes.

Thermal resistivity, as calculated above, serves as a predictor for thermal stability, i.e., it is inversely proportional to geometrical change caused by thermal treatment. Thermal resistivity calculated as a function of the length of the tubes and the

experimentally obtained diameter thermal reduction are plotted in Figure S3 in the Supporting Information. This figure shows that the thermal resistivity, modelled by Equations (3) and (4), is inversely correlated to the thermal stability. Moreover, this result confirms that perforations and length increase the thermal stability of strained SiN_x structures.

In addition to the RTA treatments, tubes were covered in thin sputtered gold and electrically stimulated to mimic local heating effects that would occur in device level operation. Only the solid and uniformly perforated tubes were tested. The gradually and abruptly perforated tubes likely would reduce slowly, possibly without a noticeable cutoff. The rectangularly perforated tubes were not tested because their thermal breakdown was not found; in the ranges tested, they collapsed entirely. The goal of this study was to provide a point of comparison to the RTA study. Without a reliable thermal study for them, they cannot be truly compared with an electrical stimulation study.

Voltage was swept in a probe station setup as schematized in **Figure 3**a. All stimulated tubes exhibited a breakdown voltage, characteristic of a fuse, as shown in their *I*–*V* characteristics (Figure 3b). Similar to the thermal treatment, the tubes electrically treated underwent similar geometry deformation, i.e., the tubes reduced in diameter and rolled further as shown in Figure 3c. This geometrical change led to breakage in the Au layer between that covering the tube wall and the planar film. Prior to the electrical treatment, the Au layer was fully continuous over the topography of the array of tubes (Figure 3d), allowing current to flow through the tube and heat it up. Once the tube diameter started to shrink as the current induced heat increased, the stress at the conjunction between the planar gold film and the gold film that was conformally coated on the tube wall increased. When the stress built up to the point of catastrophic physical breakage (Figure 3e), the current stopped flowing through the tube. Instead, current flowed through the gold layer surrounding the tube. After breakdown, the resistance increased significantly, leading to nearly no current (>100 nA) to flow through the structure. The fuse operated with less than 10 mΩ resistance on, and achieved 5 kΩ resistance after breakdown, making it competitive with similarly sized fuses.[32]

Analysis of the electrical characteristics is modelled as two resistors in parallel, the resistance of the gold sheet (R_{film}) and the tubular structure (R_{tube}) (Figure 3a). The resistance of the gold sheet was measured separately and used for further calculation. Using a trapezoidal integration technique to sum the power of the *I*–*V* curves (described in detail in the Supporting Information), it was calculated that the solid tubes

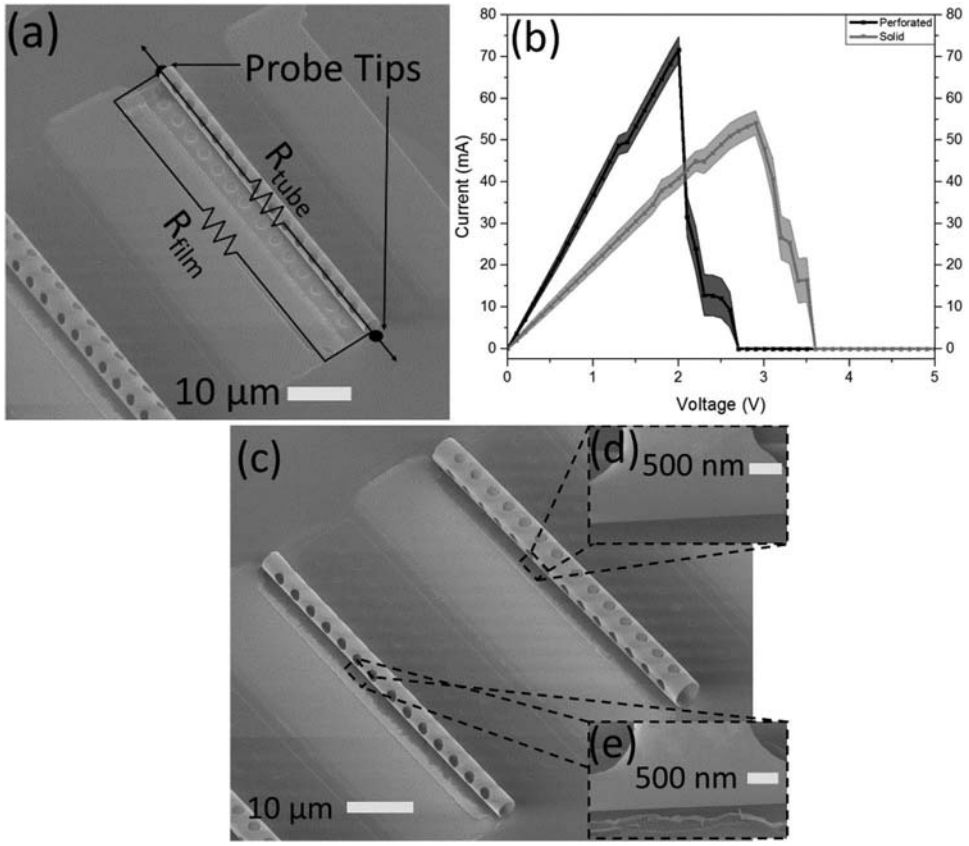

Figure 3. a) Probe layout and equivalent circuit of electrical stimulation test overlaid on an image of electrically stimulated tube. b) *I*–*V* characteristics for electrically stimulated thermal reduction of perforated and solid tubes, with continuous error bars. Perforated one shows higher rated current at a fixed voltage and lower breakdown voltage. c) A comparison of an electrically treated tube (bottom left) adjacent to an untreated tube (top right). d) Gold layer is intact without treatment. e) Gold layer is broken as a result of the tube diameter reduction after treatment.

were exposed to 223.6 J of heat and the perforated tubes were exposed to 104.7 J in heat.

Given the specific heat density of PECVD SiN_x and the volume of the tubes, the solid tubes were exposed to an average of 555 °C before breakdown, and the perforated tubes were exposed to 616 °C before breakdown voltage was reached, assuming that all energy was dissipated as heat energy. These temperatures are higher than those found in the RTA experiments; this discrepancy is likely caused by the added gold on the substrates, which would increase their thermal threshold by more effectively dissipating heat. The Au film likely did not contribute to the mechanical stress as its absolute stress should be well below 100 Pa,[33] significantly lower than that of the SiN_x layers. Additionally, the overall exposure time was far shorter than it was in the RTA treatment. With those caveats in mind, these results are consistent with the results of the RTA testing, namely that solid tubes cannot withstand as much heat as their perforated counterparts. Note that the perforated tubes have consequentially more resistance than the solid tubes, leading to their lower threshold voltage. Their higher resistance corresponds to a larger thermal treatment overall, making these initial results consistent with the RTA results.

This study explored using geometrical perforation of membranes to manipulate the thermal properties of S-RuM structures. With the additions of perforation, thermal resistance increased dramatically. Depending on the perforation pattern, which can be readily controlled by lithography, thermally induced deformation of SiN_x-based S-RuM structure occurs in the form of diameter shrinkage, either locally or globally, with increasing temperature. As much as 120 °C difference in thermal breakdown temperature has been demonstrated. Additionally, it has also been demonstrated that electrical current induced heating of an array of S-RuM tubes conformally coated with a continuously layer of metal manifested as fuses when the deformation of the tubes led to catastrophic electrical breakage. Similar to the thermally induced deformation, perforation increases the thermal resistance thus a higher rated current. S-RuM structures as an emerging self-assembled 3D architecture platform through 2D processing, have already been well understood in their formation mechanism at all scales[33,34] and used for a wide range of applications, including in passive electronics,[6,7,11–13] optical measurement and sensing,[15–18,35,36] and biological cell growth.[5,37,38] This work represents advancement in the manipulation of these structures for thermal management, which is critical to applications in the field of 3D microelectromechanical systems. Because of the free-standing nature of 3D structures, the thermal effect can be manipulated with larger amplitude through air perforation. Air perforations have been used in other works to mimic biological microvasculatures[38] and as filtration systems for oil/water emulsifications.[39] Combined with the maturity of lithographical patterning and thus the vast types of geometrical perforation schemes possible, both in plane and after rolled-up, this work opens up new possibilities of device applications that are thermally sensitive such as phase change material-based sensing, logic, and memory on-chip and in package, with unprecedented versatility. For example, future work can utilize the techniques demonstrated herein to embed a high performance, single-use, tunable fuse with a minimized footprint.[32]

Experimental Section

S-RuM Fabrication: The S-RuM microtubes used in this study were fabricated with previously-established S-RuM fabrication techniques.[2,5,6] Briefly, a 20 nm germanium (Ge) sacrificial layer was deposited on a <100> silicon wafer using electron beam evaporation (CHA SEC-600, E-Beam Evaporator). This layer was followed by 20 nm of LF silicon nitride (SiN_x) and 20 nm of HF silicon nitride (SiN_x) by plasma-enhanced chemical vapor deposition (STS Mixed-Frequency PECVD System) at 380 kHz and 13.56 MHz, respectively, providing the required stress for self-rolling. Samples were subsequently photolithographically patterned (AZ 5214E photoresist and Karl Suss MJB3 Contact Mask Aligner) with arrays of rectangular mesas, defined with a reactive ion etch (PlasmaLab Freon/O_2 Reactive Ion Etching (RIE) System). One end of the rectangular mesas suspended using photolithographically-aligned silicon dioxide (SiO_2) anchors, which were deposited with PECVD (PlasmaLab PECVD System). Finally, the Ge sacrificial layer was removed with a wet chemical etch of hydrogen peroxide (H_2O_2) for 90 min at 80 °C, thereby releasing the membrane structures from the substrate, which spontaneously rolled up into microtubes. All the perforated structures have the same 2D dimensions – 61 µm wide and 17 µm long rectangular strips but varied in the perforation patterns. Nonperforated solid tubes with varying lengths were fabricated to study the length effect on thermal breakdown.

S-RuM Thermal Treatment: Samples were thermally treated with rapid thermal annealing (RTA; Jipelec Rapid Thermal Processor) to a range of temperatures at a ramp rate of 8.33 °C s^{-1} for 3 min. In addition, the microtubes were treated using an electrical current in a probe system (4200A-SCS Paramater Analyzer) to simulate the effect observed in the annealing experiment. Samples were allowed at least one hour after treatment to stabilize before imaging and were used for only one temperature cycle each.

S-RuM Electrical Treatment: SiN_x S-RuM tubes were exposed to a range of electrical currents to exhibit the same effects as RTA. For this experiment, untreated samples, prepared in the same manner as before, were sputter-coated with a thin layer (30 nm) of gold (Au). The Au layer covered the entire sample surface conformally, including the inside edges of the tubes, forming continuous current flow paths from end to end along the tube axis and with the planar film in between the tubes. The samples were then individually electrically stimulated using a Keithley [4200A-SCS] Parameter Analyzer with current passing through the tube from one opening to the other, as seen in Figure 3a. Voltage was swept at 0.588 V s^{-1} up to a maximum of 5 V.

Control Experiment Preparation: Two 4 in. silicon wafers were used to directly measure the change in film stress using the same thermal annealing methodology described above as a control experiment. On one wafer was deposited 20 nm of LF SiN_x: the other with 20 nm of HF SiN_x. Annealing was carried out at 350 °C for 5 min at a ramp rate of 8.25 °C s^{-1}. The samples' stress were measured using a film stress measurement system (FSM 500TC) after film deposition and following annealing.

Supporting Information

Supporting Information is available from the Wiley Online Library or from the author.

Acknowledgements

The work was supported in part by NSF EEC #1449548 (J.M., X.L.), and NSF IIP #1701047 (D.W., W.H., X.L.) by the U.S. Department of Energy, Office of Basic Energy Sciences, Division of Materials Sciences and Engineering, under Award DE-FG02-07ER46471 (P.F., X.L.).

Conflict of Interest

The authors declare no conflict of interest.

Keywords

perforation, self-rolled-up membrane, silicon nitride membrane, thermal breakdown

Received: June 7, 2019
Revised: August 3, 2019
Published online: September 8, 2019

[1] X. Li, *J. Phys. D: Appl. Phys.* **2008**, *41*, 193001.
[2] P. Froeter, X. Yu, W. Huang, F. Du, M. Li, I. Chun, S. H. Kim, K. J. Hsia, J. A. Rogers, X. Li, *Nanotechnology* **2013**, *24*, 475301.
[3] S. Böttner, M. R. Jorgensen, O. G. Schmidt, *Scr. Mater.* **2016**, *122*, 119.
[4] Y. Mei, G. Huang, A. A. Solovev, E. B. Ureña, I. Mönch, F. Ding, T. Reindl, R. K. Y. Fu, P. K. Chu, O. G. Schmidt, *Adv. Mater.* **2008**, *20*, 4085.
[5] P. Froeter, Y. Huang, O. V. Cangellaris, W. Huang, E. W. Dent, M. U. Gillette, J. C. Williams, X. Li, *ACS Nano* **2014**, *8*, 11108.
[6] W. Huang, X. Yu, P. Froeter, R. Xu, P. Ferreira, X. Li, *Nano Lett.* **2012**, *12*, 6283.
[7] J. Pu, X. Wang, R. Xu, S. Xu, K. Komvopoulos, *Microsyst. Nanoeng.* **2018**, *4*, 1.
[8] A. B. Sachid, M. Tosun, S. B. Desai, C. Y. Hsu, D. H. Lien, S. R. Madhvapathy, Y. Z. Chen, M. Hettick, J. S. Kang, Y. Zeng, J. H. He, E. Y. Chang, Y. L. Chueh, A. Javey, C. Hu, *Adv. Mater.* **2016**, *28*, 2547.
[9] B. S. Schulze, G. Huang, M. Krause, D. Aubyn, V. A. Bolaños Quiñones, C. K. Schmidt, Y. Mei, O. G. Schmidt, *Adv. Eng. Mater.* **2010**, *12*, B558.
[10] S. Alben, B. Balakrisnan, E. Smela, *Nano Lett.* **2011**, *11*, 2280.
[11] X. Yu, W. Huang, M. Li, T. M. Comberiate, S. Gong, J. E. Schutt-Aine, X. Li, *Sci. Rep.* **2015**, *5*, 9661.
[12] D. D. Karnaushenko, D. Karnaushenko, H. J. Grafe, V. Kataev, B. Büchner, O. G. Schmidt, *Adv. Electron. Mater.* **2018**, *4*, 1.
[13] W. Huang, J. Zhou, P. J. Froeter, K. Walsh, S. Liu, M. D. Kraman, M. Li, J. A. Michaels, D. J. Sievers, S. Gong, X. Li, *Nat. Electron.* **2018**, *1*, 305.
[14] X. Yu, E. Arbabi, L. L. Goddard, X. Li, X. Chen, *Appl. Phys. Lett.* **2015**, *107*, 031102.
[15] G. S. Huang, S. Kiravittaya, V. A. Bolaños Quiñones, F. Ding, M. Benyoucef, A. Rastelli, Y. F. Mei, O. G. Schmidt, *Appl. Phys. Lett.* **2009**, *94*, 2007.
[16] F. Li, Z. Mi, S. Vicknesh, *Opt. Lett.* **2009**, *34*, 2915.
[17] Z. Mi, P. Bianucci, *Curr. Opin. Solid State Mater. Sci.* **2012**, *16*, 52.
[18] W. Huang, S. Koric, X. Yu, K. J. Hsia, X. Li, *Nano Lett.* **2014**, *14*, 6293.
[19] C. C. Bof Bufon, J. D. Cojal González, D. J. Thurmer, D. Grimm, M. Bauer, O. G. Schmidt, *Nano Lett.* **2010**, *10*, 2506.
[20] S. Giudicatti, S. M. Marz, L. Soler, A. Madani, M. R. Jorgensen, S. Sanchez, O. G. Schmidt, *J. Mater. Chem. C* **2014**, *2*, 5892.
[21] A. Madani, S. Böttner, M. R. Jorgensen, O. G. Schmidt, *Opt. Lett.* **2014**, *39*, 189.
[22] T. J. Cotler, J. Chapple-Sokol, *J. Electrochem. Soc.* **1993**, *140*, 2071.
[23] C. Yang, J. Pham, *Silicon* **2018**, *10*, 2561.
[24] W. Li, Z. Kang, Y. Ye, Y. Jiang, *5th Int. Symp. Adv. Opt. Manuf. Test. Technol. Optoelectron. Mater. Devices Detect. Imager, Display, Energy Convers. Technol.* **2010**, *7658*, 765824.
[25] D. W. Hess, *J. Vac. Sci. Technol., A* **1984**, *2*, 244.
[26] H.-Y. Yan, K.-S. Ou, K.-S. Chen, *Strain* **2008**, *44*, 259.
[27] C. Yang, Y. Huang, H. Cheng, L. Jiang, L. Qu, *Adv. Mater.* **2018**, *1805705*, 1.
[28] D. L. Smith, *J. Vac. Sci. Technol. B: Microelectron. Nanometer Struct.* **1990**, *8*, 551.
[29] P. J. French, P. M. Sarro, R. Mallée, E. J. M. Fakkeldij, R. F. Wolffenbuttel, *Sensors Actuators, A* **1997**, *58*, 149.
[30] F. Incropera, D. Dewitt, T. Bergman, A. Lavine, *Principles of Heat and Mass Transfer*, John Wiley & Sons, NJ **2011**.
[31] J. Kuntner, A. Jachimowicz, F. Kohl, B. Jakoby, *Proc. Eurosensors Conf.* **2006**, *2*, 388.
[32] N. Robson, J. Safran, C. Kothandaraman, A. Cestero, X. Chen, R. Rajeevakumar, A. Leslie, D. Moy, T. Kirihata, S. Iyer, *Proc. IEEE 2007 Cust. Integr. Circuits Conf.* **2007**, 799.
[33] R. Abermann, R. Koch, *Thin Solid Films* **1985**, *129*, 71.
[34] H. Wang, H. Zhen, S. Li, Y. Jing, G. Huang, Y. Mei, W. Lu, *Sci. Adv.* **2016**, *2*, e1600027.
[35] P. Bianucci, S. Mukherjee, P. Poole, Z. Mila, *2011 IEEE Winter Top. WTM 2011*, IEEE, NJ **2011**, pp. 127–128.
[36] O. V. Cangellaris, E. A. Corbin, P. Froeter, J. A. Michaels, X. Li, M. U. Gillette, *ACS Appl. Mater. Interfaces* **2018**, acsami.8b10233.
[37] M. Yu, Y. Huang, J. Ballweg, H. Shin, M. Huang, D. E. Savage, M. G. Lagally, E. W. Dent, R. H. Blick, J. C. Williams, *ACS Nano* **2011**, *5*, 2447.
[38] R. Arayanarakool, A. K. Meyer, L. Helbig, S. Sanchez, O. G. Schmidt, *Lab Chip* **2015**, *15*, 2981.
[39] Y. Zhu, D. Wang, L. Jiang, J. Jin, *NPG Asia Mater.* **2014**, *6*, e101.

